UiT The Arctic University of Norway

Faculty of Science and Technology

Department of Physics and Technology

Wideband Self-Interference Cancellation Using Multi-Tap Filter in Radar Front End

Bendik Heiskel

FYS-3941 Master's thesis in applied physics and mathematics 30 SP

Abstract

The largest hurdle in full duplex wireless systems is the self-interference introduced by the transmitted signal into the received signal. In multi antenna systems this interference is caused by the direct coupling between the transmitting and receiving antennas. In systems where the transmitter and receiver uses the same antenna the interference is caused by inadequate isolation between the transmitter and receiver front-ends. In most systems the transmitted power is orders of magnitude higher than the received signal power. This causes the interference to saturate the receiver and can damage the receiver. One way of reducing this interference is to include a filter in the microwave front-end. This filter uses the transmitted signal to generate an inverse of the interference and adds it to the receiver signal path.

In this thesis a multi-tap self-interference cancellation filter is designed, optimized and fabricated. The filter parameters are optimized using the basin-hopping algorithm combined with the Nelder-Mead downhill simplex algorithm. The filter is a multi-tap filter, where each tap contains phase shift, attenuation and delay elements. The filter is experimentally verified to reduce the self interference by 10.45 dB over a frequency band from 1GHz to 3GHz.

Contents

List of Figures

Abbreviations

SIC Self-interference cancellation

SI Self-interference

UWB Ultra wide band

Tx transmitting

Rx receiving

RF radio frequency

VNA Vector Network Analyzer

Selected Symbols

Constants

ϵ_0	Absolute permittivity of vacuum	$8.85 \cdot 10^{-12}\mathrm{Fm}^{-1}$
μ_0	Absolute permeability of vacuum	$4\pi \cdot 10^{-7}\mathrm{Hm}^{-1}$
c	Speed of light in vacuum	$299792458\mathrm{ms}^{-1}$
η_0	Free-space wave impedance	376.73Ω

Chapter 1

Introduction

1.1 Simultaneous transmit and receive system

Radar and radio systems usually operate in half duplex mode. This means that the system transmits or receive signals, but not both simultaneously. These systems use two different methods, separating the Tx and Rx signals by time, i.e only transmitting or receiving at one time, or separating the Tx and Rx signals by frequency, i.e transmitting and receiving on different frequency channels. These methods are both used in radio systems, but for radar the Tx and Rx is in the same frequency range, by the operating principles of the system [1].

Simultaneous transmit and receive systems operate in-band full-duplex mode, by transmitting and receiving in the same frequency channel at the same time. For this to be possible, the system must achieve sufficient cancellation of the self-interference produced by the transmitting and receiving link.

1.2 Self-interference cancellation

Self-interference cancellation is the process of canceling the self-interference present in STAR-systems. The main methods used for reducing the SI are high isolation antennas, active SIC-filters and passive SIC-filters [2], [3], [4] .

By utilising a combination of these techniques, a high cancellation can be achieved.

1.3 Structure of Thesis

The thesis is divided into four parts:

Part 1 contains the background theory for the methods described in this thesis. Chapter 2 presents the transmission lines utilized in the implemented filter. This includes fundamental equations used in microstrip and stripline construction. Chapter 3 describes the main methods of self-interference cancellation, where the multi-tap filter is the filter implemented in the thesis. Chapter 4 presents the microstrip devices including power dividers, directional couplers, phase shifters and delay lines. Chapter 5 presents the numerical optimization

techniques used for filter optimization. The optimization method used for structural optimization of the microstrip circuits is also described.

In **Part 2** the methodology for the construction of the Tx-module and the filter-module. Chapter 7 presents the Tx-module in which the transmitted signal is split to 4 antennas and the received signal from the antennas are combined. A part of the signal is also extracted for the filter-module. In chapter 8 the optimization of the filter parameters is presented. In Chapter 9 the filter-module in which the filter response is generated.

Part 3 contains the simulated and measured results. The results related to the Tx-module is presented in chapter 11. The filter-module along with the filter optimization results is presented in chapter 13. Chapter 14 contains the complete system results.

In **Part 4** the conclusions are drawn.

Part I

Background theory

Chapter 2

Transmission lines

2.1 Stripline

Stripline transmission lines consist of a planar conductor between two ground planes, where the space between the ground planes is filled with a dielectric medium. In the most basic type of stripline construction, the conductor is centered between the ground planes. Since the wave propagates in a homogeneous medium the transmission line supports full TEM wave propagation. The phase velocity, propagation constant and characteristic impedance is calculated using the well known equations from [5]:

$$v_p = \frac{1}{\sqrt{\mu_0 \epsilon_0 \epsilon_r}} = \frac{c}{\sqrt{\epsilon_r}} \tag{2.1}$$

$$\beta = \frac{\omega}{v_p} \tag{2.2}$$

$$Z_0 = \frac{1}{v_p C}, \tag{2.3}$$

where C is the capacitance per unit length of the line. The capacitance of the transmission line is given by the width of the conductor and the distance between the ground planes. Assuming a conductor with zero thickness the characteristic impedance can be calculated to 1% of the actual value using the equations from [6]:

$$Z_0 = \frac{30\pi}{\sqrt{\epsilon_r}} \frac{b}{W_e + 0.441b} \tag{2.4}$$

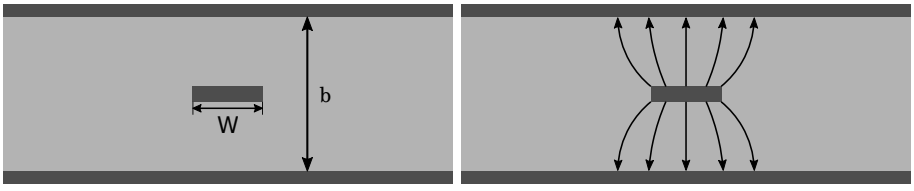

Figure 2.1: Stripline transmission line. (a) Geometry. (b) Electric field

$$\frac{W_e}{b} = \begin{cases} \frac{W}{b} & \text{, for } \frac{W}{b} > 0.35 \\ \frac{W}{b} - \left(0.35 - \frac{W}{b}\right)^2 & \text{, for } \frac{W}{b} < 0.35 \end{cases} \tag{2.5}$$

For a given characteristic impedance :

$$\frac{W}{b} = \begin{cases} \frac{30\pi}{\sqrt{e_r} Z_0} & \text{, for } \sqrt{e_r} Z_0 < 120\Omega \\ 0.85 - \sqrt{0.6 - \frac{30\pi}{\sqrt{e_r} Z_0}} & \text{, for } \sqrt{e_r} Z_0 > 120\Omega \end{cases} \tag{2.6}$$

2.2 Microstrip

Microstrip line is a transmission line consisting of a printed conductor and ground separated by a substrate. Without the presence of the dielectric substrate the transmission line would be a simple two wire transmission line with a strip conductor over a ground plane in a homogeneous medium. This would be a TEM transmission line, with phase velocity $v_p = c$.

When the dielectric substrate is present the electric and magnetic field is not contained in a homogeneous region. This makes the microstrip transmission line not capable of supporting TEM waves. When the dielectric substrate is electrically thin ($d << \lambda$) the fields are quasi-TEM. By using substrates with high permittivity, more of the fields are contained in the substrate and more of a homogeneous transmission medium, this makes the waves closer to TEM waves. Since the transmission line supports quasi-TEM waves, the phase velocity, propagation constant and characteristic impedance can be approximated from the quasi-static solutions. The phase velocity and propagation constant are then expressed as:

$$v_p = \frac{1}{\sqrt{\mu_0 \epsilon_0 \epsilon_e}} = \frac{c}{\sqrt{\epsilon_e}} \tag{2.7}$$

$$\beta = \frac{\omega}{v_p} \tag{2.8}$$

where ϵ_e is the effective dielectric constant. The effective dielectric constant represents a homogeneous medium that replaces the air and substrate. By doing this, the phase velocity and propagation constant are calculated by equations (2.7) and (2.8). A equation for the effective dielectric constant was first introduced by [7] then modified by [8]:

$$\epsilon_e = \frac{1}{2}\left[\epsilon_r + 1 + (\epsilon_r - 1)F\right] \tag{2.9}$$

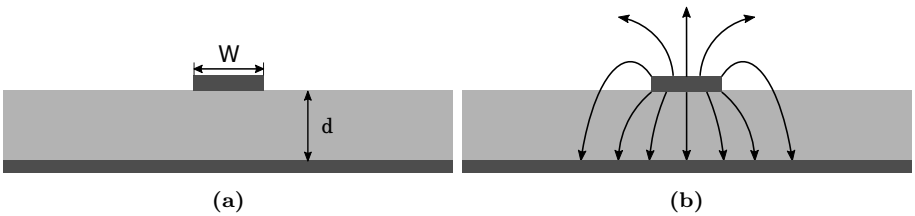

Figure 2.2: Microstrip transmission line. (a) Geometry. (b) Electric field

$$F = \begin{cases} \sqrt{1 + 12\frac{d}{w}} + 0.04\left(1 - \frac{w}{d}\right)^2 & \text{, when } \frac{w}{d} \leq 1 \\ \sqrt{1 + 12\frac{d}{w}} & \text{, when } \frac{w}{d} \geq 1 \end{cases} \tag{2.10}$$

The characteristic impedance of the microstrip is then given by the width and thickness of the conductor, the thickness of the substrate and the effective dielectric constant of the substrate. An equation for approximating the characteristic impedance was proposed by [9] and later improved to within 1% accuracy by [8]:

$$Z_0 = \begin{cases} \frac{\eta_0}{2\pi\sqrt{\epsilon_e}} ln\left(\frac{8d}{w} + \frac{w}{4d}\right) & \text{, when } \frac{w}{d} \leq 1 \\ \frac{\eta_0}{\sqrt{\epsilon_e}\left[\frac{w}{d} + 1.393 + 0.667 ln\left(\frac{w}{d} + 1.444\right)\right]} & \text{, when } \frac{w}{d} \geq 1. \end{cases} \tag{2.11}$$

where $\eta_0 = 376.73\Omega$ is the free-space wave impedance For a given characteristic impedance the w/d ratio is calculated as:

$$\frac{w}{d} = \begin{cases} \frac{8}{e^A - 2e^{-A}} & \text{, when } \frac{w}{d} \leq 2 \\ \frac{2}{\pi}\left[\begin{array}{l} \mathrm{B} - 1 - \ln(2\mathrm{B} - 1) \\ + \frac{\epsilon_r - 1}{2\epsilon_r}\left(\ln(\mathrm{B} - 1) + 0.39 - \frac{0.61}{\epsilon_r}\right) \end{array}\right] & \text{, when } \frac{w}{d} \geq 2 \end{cases} \tag{2.12}$$

where

$$A = \frac{2\pi Z_0}{\eta_0}\sqrt{\frac{\epsilon_r + 1}{2}} + \frac{\epsilon_r - 1}{\epsilon_r + 1}\left(0.23 + \frac{0.11}{\epsilon_r}\right) \tag{2.13}$$

$$B = \frac{\pi\eta_0}{w\sqrt{\epsilon_r} Z_0} \tag{2.14}$$

Chapter 3

Methods of self-interference cancellation

There are two main methods to remove the transmitted signal from the received signal. One method involves digitally removing a reference signal from the received signal to cancel out the self-interference (SI). While the other method involves using a filter in the receiver front-end which generates the inverse of the SI and adds it to the received signal [10].

By subtracting a reference signal consisting of only the SI, a near perfect SI cancellation (SIC) can be achieved. This method could be used in systems where the power of the transmitted signal is close to the received signal and little to none amplification is needed on the receiver front-end.

In systems where the power of the received signal is low, an amplification stage is necessary on the receiver front-end. In this case the power of the transmitted signal can be orders of magnitude higher than the received signal, and the power of the SI can saturate the receiver and information contained in the received signal is lost. To prevent receiver saturation, a cancellation stage could be added to the signal path before the amplification. This stage would consists of a filter in which a part of the transmitted signal is used to generate the inverse response to the SI and add it in to the signal path.

3.1 Digital SIC-filtering

Digital SIC-filtering filters out the SI in the digital domain. A reference signal for the system is recorded and subtracted from the received signal to remove the SI. The reference signal could be measured by transmitting and recording the received signal without any information other than the SI.

3.2 Multi-tap filtering

Multi-tap filters split the signal into multiple parts performing different filtering on each tap and adding the taps back together.

A basic multi-tap filer used in SIC could consist of delay and attenuation elements. This results in $2N$ degrees of freedom, where N is the number of taps.

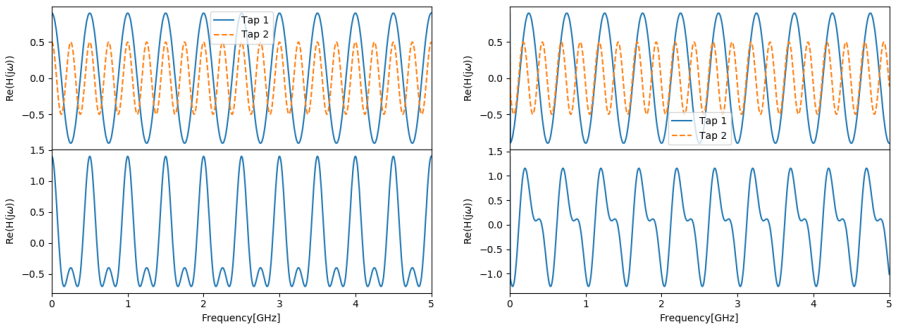

(a) **(b)**

Figure 3.1: (a) Simulated frequency domain response of a 2 tap filter.

The impulse response of this filter, with for each tap an α_k attenuation ratio and τ_k delay.

$$h_{\text{canc}}(t) = \sum_{k=1}^{K} \alpha_k \delta(t - \tau_k) \tag{3.1}$$

By adding phase shift the cancellation can be improved, by allowing a finer tuning of the individual impulses generated by the taps. The time domain response for a multi-tap filter with phase shift:

$$h_{\text{canc}}(t) = \sum_{k=1}^{K} \alpha_k \delta(t - \tau_k) * \left(\cos\phi_k \delta(t) + \sin\phi_k \frac{1}{\pi t} \right) \tag{3.2}$$

where α_k, ϕ_k and τ_k are the attenuation ratio, phase shift, and time delay for tap k, respectively.

In the frequency domain we get:

$$H_{\text{canc}}(j\omega) = \sum_{k=1}^{K} \alpha_k * e^{-j\omega\tau_k} e^{-j\phi_k \text{sgn}(\omega)} \tag{3.3}$$

where

$$\text{sgn}(\omega) = \begin{cases} 1 & \text{, if } \quad \omega \geq 0 \\ -1 & \text{, if } \quad \omega < 0. \end{cases} \tag{3.4}$$

To implement this kind of filter, power dividers are used to split the signal for each tap. The attenuation, phase shift and time delay components of the filter are realized using resistive attenuator, microstrip phase shifters, and stripline delay lines. By using power dividers with unequal split, only the required power is sent to each tap negating the need for resistive attenuators in addition to the power splitter.

Chapter 4

Microwave Devices

4.1 Power splitter and combiners

4.1.1 Resistive dividers

Resistive power dividers are divider circuits utilising resistive loads to divide the power and match the ports.

Unequal power dividers

The resistive unequal power divider presented in [11] is based on a resistive T-pad attenuator,where a voltage divider is substituted for the resistor to ground. The resistances, Rs and Rp from figure 4.1a are calculated using:

$$\frac{\mathrm{Rs}}{Z_0} = \frac{1-\alpha}{1+\alpha} \tag{4.1}$$

$$\alpha = 10^{-\mathrm{dB}_1/20} \tag{4.2}$$

$$\frac{\mathrm{Rp}}{Z_0} = \frac{1-\mathrm{Rs}^2}{2\mathrm{Rs}}, \tag{4.3}$$

where dB_1 is the desired attenuation on port 2, and Z_0 is the characteristic impedance.

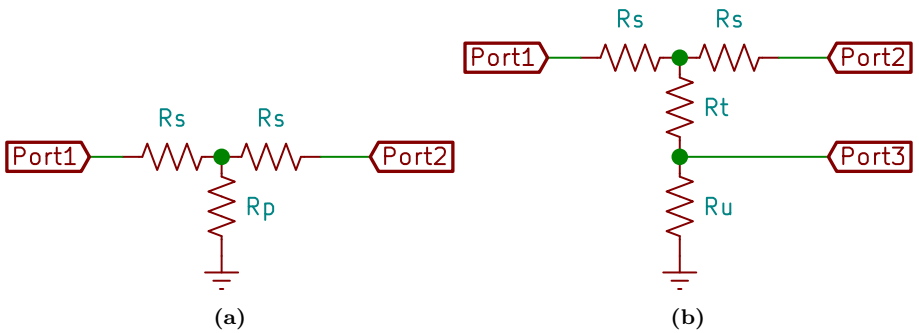

Figure 4.1: (a) T pad attenuator circuit. (b) Unequal resistive power divider circuit

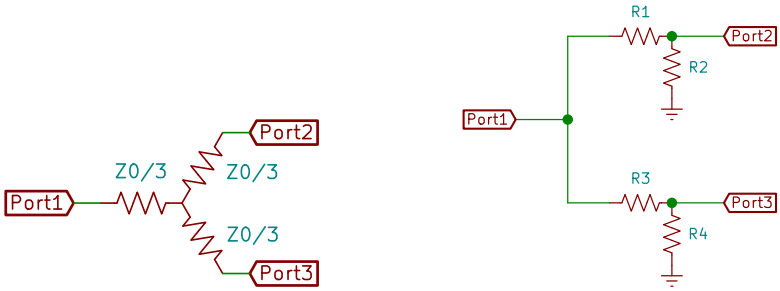

Figure 4.2: (a) Three port Wye power divider. (b) Three port owens power divider

The resistances Rt and Ru are given by Rp:

$$\frac{\mathrm{Ru}}{Z_0} = \sqrt{\frac{1}{1 - \frac{4}{2\mathrm{Rp}+\mathrm{Rs}+1}}} \tag{4.4}$$

$$\frac{\mathrm{Rt}}{Z_0} = \mathrm{Rp} - \frac{\mathrm{Ru}}{\mathrm{Ru}+1} \tag{4.5}$$

Wye power divider

Wye power splitters are equal split resistive dividers. The resistive loads are arranged in a star shape shown in figure 4.2a. The resistance of the loads are given by Z_0/n, where n is the number of ports. For a three port Wye power divider the output power for each port is 6dB below the input power. The Wye divider has poor isolation on S32 and S23, this is a result of the divider being reciprocal. The reciprocity also results in the divider being matched at all ports.

Owens power divider

The Owens power divider presented by [12] is a resistive power divider with high isolation between the outputs. The power divider uses two voltage dividers to split the power. This gives the divider high isolation, but it also introduces a large loss. For an equal split Owens divider, the output power is -9.56 dB below the input power, with -19.08 dB isolation. The circuit of a two-way Owen power divider is shown in figure 4.2b.

To calculate the resistor values a coupling factor is chosen for one of the ports. Then the values for R1, R2, R3 and R4 are calculated using the equations from [12]:

$$R_2 = Z_0 \frac{1 + CF_2}{1 - CF_2}$$

$$R_1 = \frac{2R_2 Z_0^2}{R_2^2 - Z_0^2}$$

$$R_3 = 2R_2 \frac{R_2 - Z_0}{2R_2 - Z0}$$

$$R_4 = \frac{R_2 Z_0}{R_2 - Z_0}$$

The coupling factors based on the resistor values are given by:

$$CF_2 = \frac{R_2 Z_0}{R_1 R_2 + R_1 Z_0 + R_2 Z_0}$$
$$CF_3 = \frac{R_4 Z_0}{R_3 R_4 + R_3 Z_0 + R_4 z_0}$$

4.1.2 Wilkinson power divider

The Wilkinson power divider was first designed in [13] using waveguides. The divider is widely used for its low loss and 3 dB power split. The structure utilizes quarter-wave transformers and a shunt resistor to match the ports while achieving isolation between the output ports. The resistor only dissipates the reflected power from the outputs. This makes the divider theoretically lossless, but in practise there is some loss introduced by the transmission lines. The characteristic impedance of the quarter-wave transformers for a 2 way divider is given by:

$$Z_1 = Z_0\sqrt{2}. \tag{4.6}$$

Since Wilkinson power dividers utilise quarter-wave impedance transformers, they are frequency dependant and have a narrow operational bandwidth. To increase the bandwidth of the Wilkinson power divider different techniques have been used including, multi section matching transformer [14], tapered transmission lines [15] and radial stub matching [16].

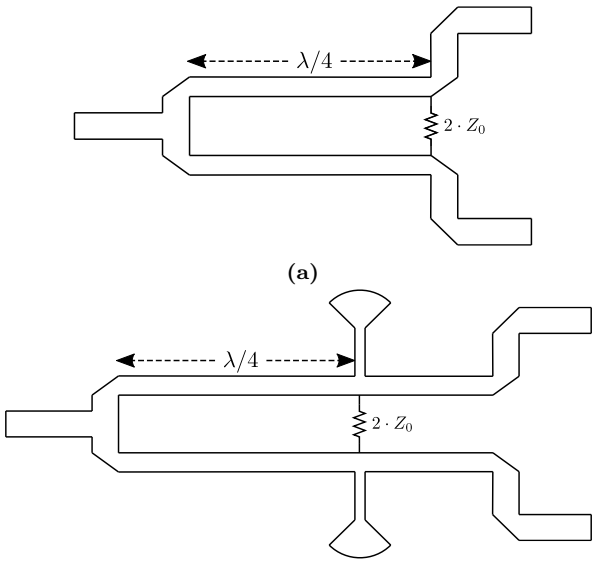

Figure 4.3: (a) Wilkinson power divider. (b) Wilkinson power divider with radial stub

Radial stub tuning

The radial stub is used in planar transmission lines, with the shape of a circular sector. Radial stubs are often used to replace low impedance stubs. The impedance of a planar transmission line decreases as the width of the line increases, this makes low impedance stubs wide and the junction with the main line poorly defined. By using radial stubs the impedance of the stub is low and the junction becomes well defined.

Low impedance stubs are used for bandstop filter, where the bandwidth is inversely proportional to the impedance of the stub.

By utilizing radial stubs in the Wilkinson power divider the functional bandwidth of the divider has been shown to increase [16].

4.2 Directional coupler

Directional couplers are power splitters/combiners that only couples power flowing in one direction. Directional couplers are networks consisting of at least three ports, an input, an isolated and an output port. The power entering the input is coupled to the output, while power entering the output is coupled to the isolated port. A directional coupler often includes a power splitter, this results in a 4-port network with two outputs.

[17] introduces a UWB directional coupler using broadside coupled lines, the coupler is constructed using multilayer microstrip structure.

4.3 Phase shifter

4.3.1 Parallel stub phase shifter

A parallel stub phase shifter, presented in [18], utilizes two stubs in parallel to create a differential phase shift. It consists of one open and one shorted stub. To increase the bandwidth of the phase shifter a quarter wavelength transformer is used to match the input impedance of the parallel stubs with the characteristic impedance of the transmission line.

4.3.2 Edge coupled line

The edge coupled line phase shifter presented in [19] has a wide range of phase shift and a broad frequency band. The structure consists of edge coupled lines with a slot in the ground plane with a floating potential, and L-shape matching networks. The matching networks increase the operational frequency bandwidth.

4.3.3 Broadside coupled line

The broadside coupled phase shifter presented in [20] is based on the multilayer directional coupler presented in [17]. The phase shifter differs from the directional coupler in that the isolated and transmitted port are replaced by open/shorted stubs. The shifter uses two identical elliptical patches coupled through an elliptical slot in the ground plane. The phase shift is dependant on

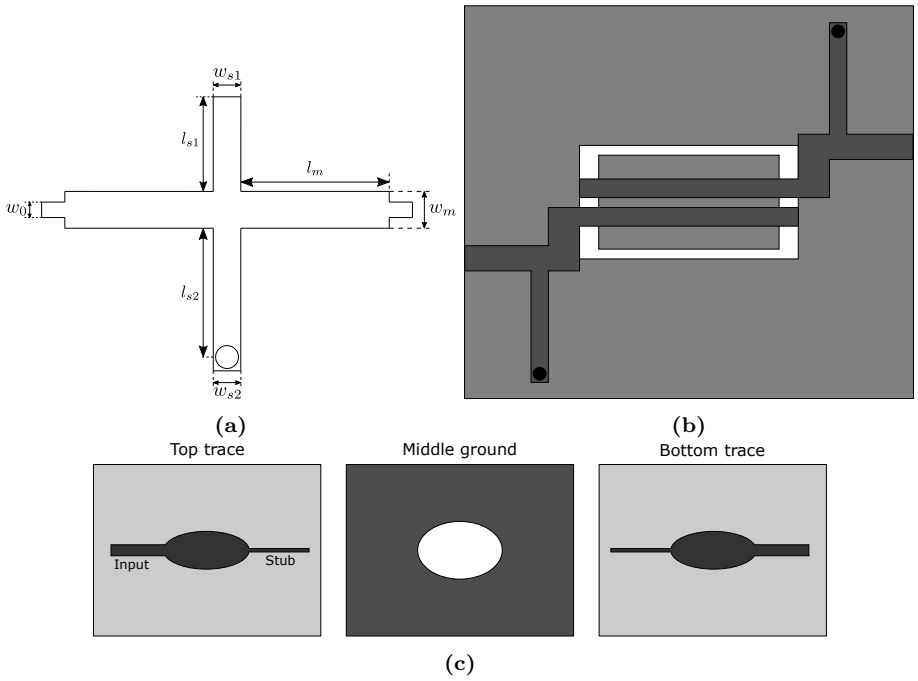

Figure 4.4: Three diagrams of phase shifters. (a) Parallel stub phase shifter. (b) Edge coupled phase shifter. (c) Multilayer broadside coupled phase shifter

the width of the patches and slot. The length of both the patches and the slot is determined by the center frequency of the frequency band the phase shifter is designed for.

4.4 Delay line

A microwave delay line is a length of transmission line in which the signal is delayed. The length of the line is determined by the desired delay and the propagation velocity of the wave in the transmission line.

4.4.1 Microstrip to Stripline

To decrease the length of the delay line and decrease radiation losses, a transition from microstrip to stripline is used.

A method for transitioning from microstrip to stripline is presented in [21]. The transition is tapered to provide a continuous characteristic impedance. For the same characteristic impedance of the microstrip line and stripline, the width of the stripline is narrower than the microstrip line. To keep constant impedance a cutout in the top ground plane over the tapered line is used.

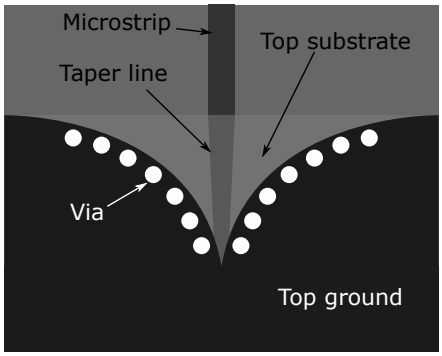

Figure 4.5: A coplanar microstrip to stripline transition

Chapter 5

Minimization techniques

5.1 Nelder-Mead

The Nelder-Mead simplex algorithm [22] is a commonly used direct search method, because of its simplicity to implement and its use of only evaluation of objective functions and no gradient evaluations. The method is a downhill simplex algorithm which only evaluates the objective function a few times per iteration. The algorithm uses a simplex with N+1 vertices which converges to the closest minimum to the initial guess. Examples of a simplex would be a triangle in 2 dimensional space and a tetrahedron in 3 dimensional space. The simplex is the simplest polytope in N dimensional space, where all vertices are of equal length. The algorithm is suited for multidimensional optimization without derivatives and constrains. The initial guess is used as the first point of the simplex and the rest is constructed from it.

The algorithm evaluates the objective function at the vertices, and orders them according to the objective function value:

$$f(x_1) \leq f(x_2) \leq ... \leq f(x_n + 1). \tag{5.1}$$

Here x_1 is the lowest evaluation of the objective function while x_{n+1} the highest. Then the centroid of the n best vertices is calculated by,

$$c = \frac{1}{n} \sum_{i=1}^{n} x_i \tag{5.2}$$

A new simplex is constructed by replacing the vertex with the highest evaluation of the objective function with a new one. The new vertex is chosen by using one of the following operations:

Reflect:

$$x_r = c + \alpha(c - x_{n+1}) \tag{5.3}$$

Expand:

$$x_e = c + \gamma(x_r - c) \tag{5.4}$$

Contract:

$$x_c = c + \beta(x_r - c), \text{ if } f_n \leq f_r < f_{n+1} \tag{5.5}$$
$$x_c = c + \beta(x_{n+1} - c) \text{ if } f_r \geq f_{n+1} \tag{5.6}$$

To determine which vertex it is replaced with, the reflected vertex of the best vertex is calculated using equation (5.3). If the evaluation of the objective function, $f_r = f(x_r)$, at the new point is in the range (f_1, f_n), the point x_{n+1} is replaced with x_r. If $f_r < f_1$ the expanded vertex is calculated using equation (5.4). If the evaluation of the objective function, $f_e = f(x_e)$, is lower than f_r the vertex x_{n+1} is replaced with x_e, otherwise replace x_{n+1} with x_r. Then the contraction is calculated using equation (5.5) or equation (5.6), depending on the value of the objective function of the reflected vertex.

The Nelder-Mead simplex is slow compared to gradient decent algorithms, but for higher dimensionality problems it is simpler to use than computing the gradient. The algorithm does also have a large dependency on the initial guess, it will converge to the closes local minimum. This makes the algorithm useful as a polishing algorithm where a faster and coarser algorithm finds the initial guess and the Nelder-Mead converges to the optimal parameters.

5.2 Basin-hopping

Basin-hopping is a algorithm which extends other minimization algorithms by running the minimization multiple times with different initial values iteratively. Where each minimization run is used to determine the change in initial values, for the next run. Given a sufficient number of iterations, the algorithm can find the global minimum for a function using for example the Nelder-Mead algorithm.

Part II

Methodology

Chapter 6

System description

The system consists of a radar front-end including a band-pass filter, unequal power splitter, hybrid coupler and two equal power splitters. A diagram of the system is shown in Fig. 6.1. The diagram shows the signal path of the front-end. The circuit is divided into two separate modules, one containing the multi-tap filter and the other containing the bandpass filter, unequal power splitter, hybrid coupler and equal power splitters.

The bandpass filter limits the transmitted UWB pulse to only frequency components within the 1-3GHz band. A unequal power divider extracts a part of the signal power which is used to construct the cancellation signal. The remaining signal is then split equally to the antennas by a directional coupler and two power dividers. The directional coupler in addition to splitting the power shift the signal to two of the antennas by 90°. The isolated port of the directional coupler receives the reflected signal measured by the four antennas. The received signal is then added with the output of the SIC-filter using a power splitter/combiner, the sum of these signals is then recorded by the transceiver electronics.

The SIC-filter used is a multi-tap filter with taps containing delay, attenuation and phase shift elements. The filter is used to filter out the part of the coupled and reflected noise generated by the directional coupler and power dividers.

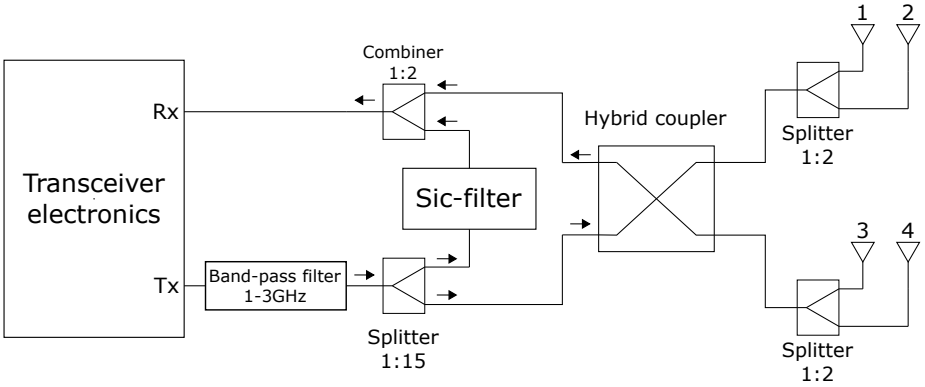

Figure 6.1: The system block diagram with signal path

Chapter 7

Tx-module design

The construction of the Tx-module consisted of four parts, the simulation of the individual devices, the schematic simulation of the complete module, combining and simulating the complete module as a complete design with microstrip lines connecting the devices. All simulation where done using CST Microwave Studio [23]. The components where all simulated and fabricated using 0.81mm Rogers RO4003C substrate.

7.1 Device selection

7.1.1 Bandpass filter

The bandpass filter used in the Tx-module has a passband of 1-3GHz. The bandpass filter uses coupled lines with capacitors and slots in the ground plane.

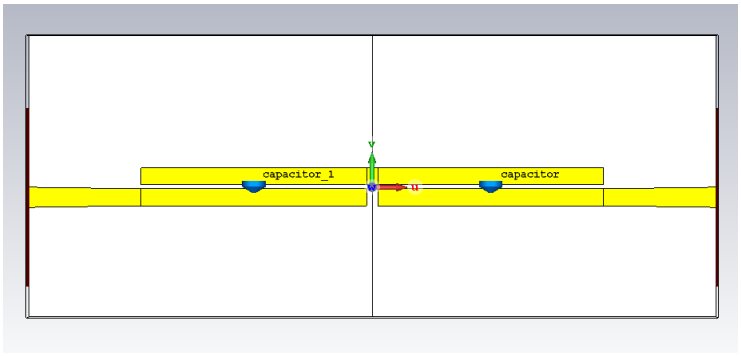

(a)

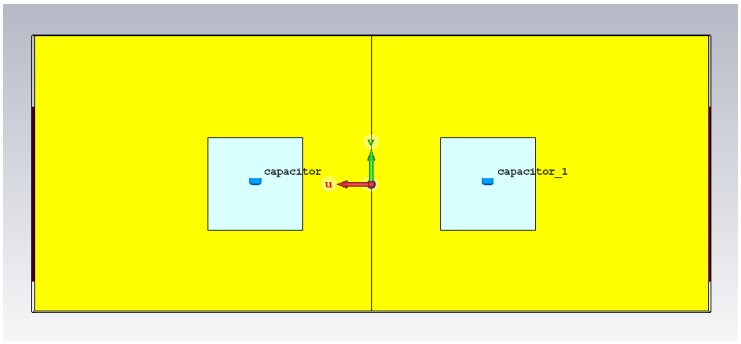

(b)

Figure 7.1

7.1.2 Unequal power divider

To extract part of the signal for the SIC-filter a unequal power divider was used with initially a 3 dB and 15 dB attenuation on the output ports. This was later changed to 4 dB and 12.25 dB attenuation based on the measured performance of the SIC-filter. The resistor values where calculated using equations (4.2) to (4.5). For a 3dB and 15dB split the resistor values Rs=8.55 Ω, Rt=111.53 Ω and Ru=77.53 Ω. These values were approximated by using E12 resistor values, Rs=10 Ω, Rt=120 Ω and Ru=82 Ω, which gives a power split of 3.5 dB and 14.5 dB.

For a 4dB, 12.25dB split the resistances are Rs=11.31 Ω, Rt=71.76 Ω, Ru=97.70 Ω. The approximated parallel resistances are:

$$\text{Rs} = \frac{15\Omega 47\Omega}{15\Omega + 47\Omega} = 11.37\ \Omega$$
$$\text{Rt} = \frac{82\Omega 560\Omega}{82\Omega + 560\Omega} = 71.53\ \Omega$$
$$\text{Ru} = \frac{100\Omega 3900\Omega}{100\Omega + 3900\Omega} = 97.50\ \Omega$$

The resulting power split using the approximated values are 4.02 dB and 12.23 dB.

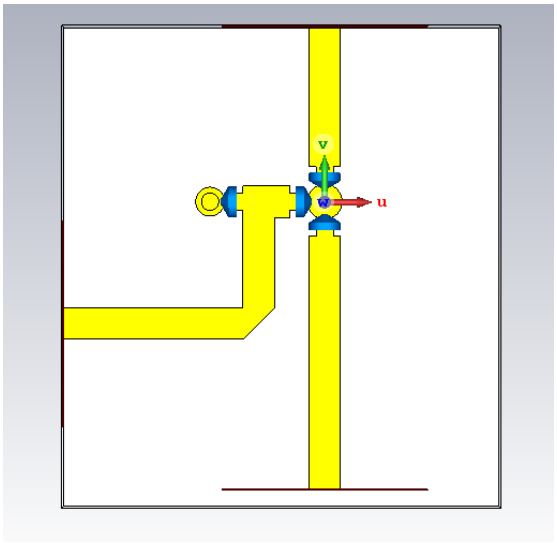

Figure 7.2

7.1.3 Directional Coupler

The directional coupler used is a UWB hybrid coupler, [17], with -3dB coupling optimized for a bandwidth for 1-3GHz.

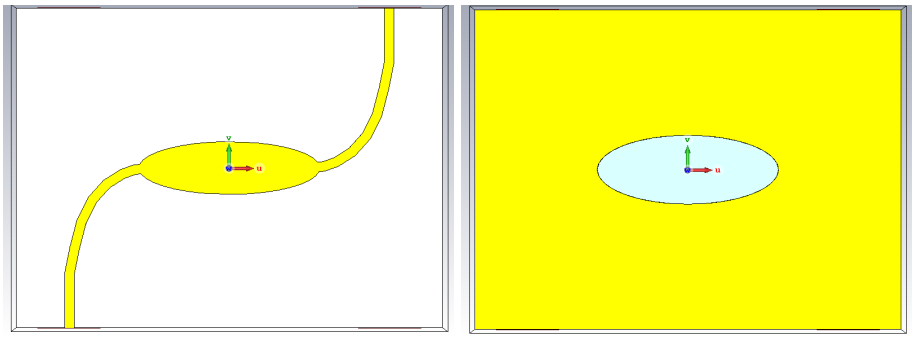

(a) **(b)**

Figure 7.3

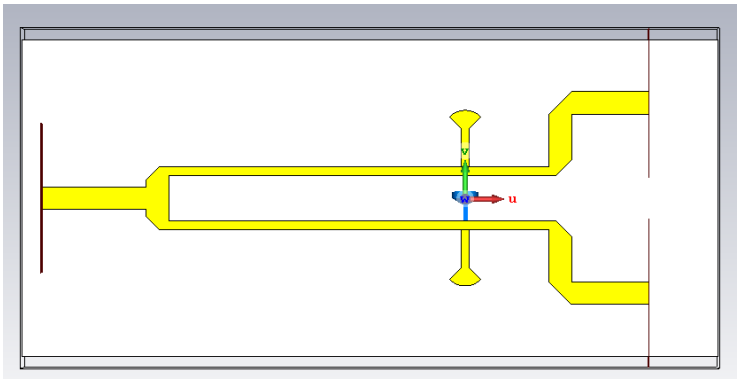

Figure 7.4

7.1.4 Power divider

Two power dividers were simulated and tested, a Wye and Wilkinson power divider. In order for the radial stubs to extend the bandwidth, the size, shape and length of the stub and line segment after the stub were optimized using CST Microwave Studio; resulting in a power divider with good performance over the frequency band 1-3GHz.

7.2 Simulation

The complete system was simulated using the schematic simulation in CST Microwave Studio. The simulation uses the S-parameter results from the individual components to construct the system.

After the S-parameter simulation the individual components where exported to Solidworks to assemble them onto a single board. The board construction was mostly dictated by the directional coupler which is a multilayer device. The components where connected with 1.8mm wide microstrip lines.

7.3 Fabricated Tx-module

The simulated Tx-module was fabricated on Rogers RO4003C substrate with a thickness of 0.81mm and a dielectric constant of 3.38.

7.3.1 Measurement setup

The fabricated board was analyzed using a Agilent FieldFox N9916A Vector Network Analyzer. To measure the S-parameters the output of the VNA was connected to the input of the TX-board, and the input of the VNA to the port under test, the remaining ports where terminated using 50 Ω loads. The board connections for the measurement of S21 is shown in figure 7.6

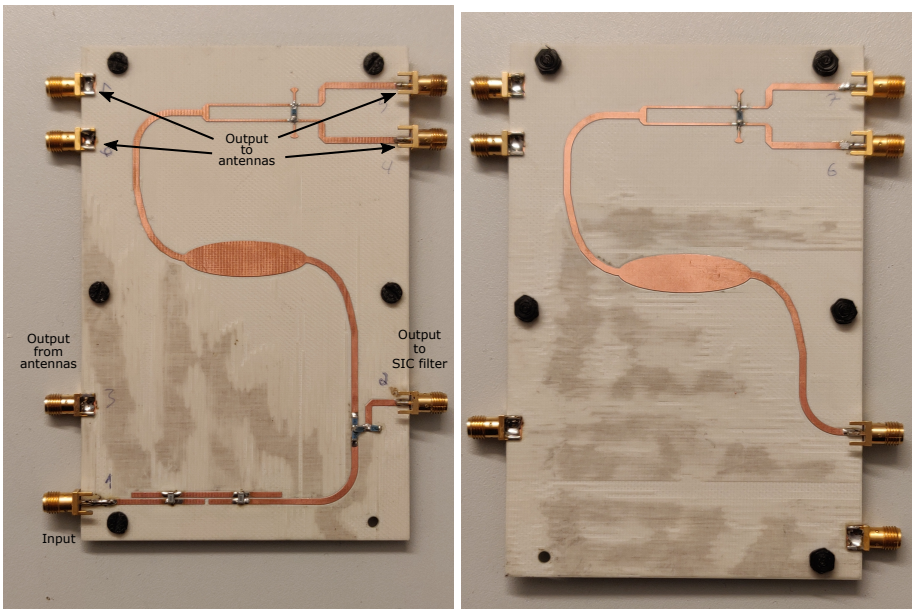

(a) **(b)**

Figure 7.5: Fabricated tx-module,(a) front and (b) back

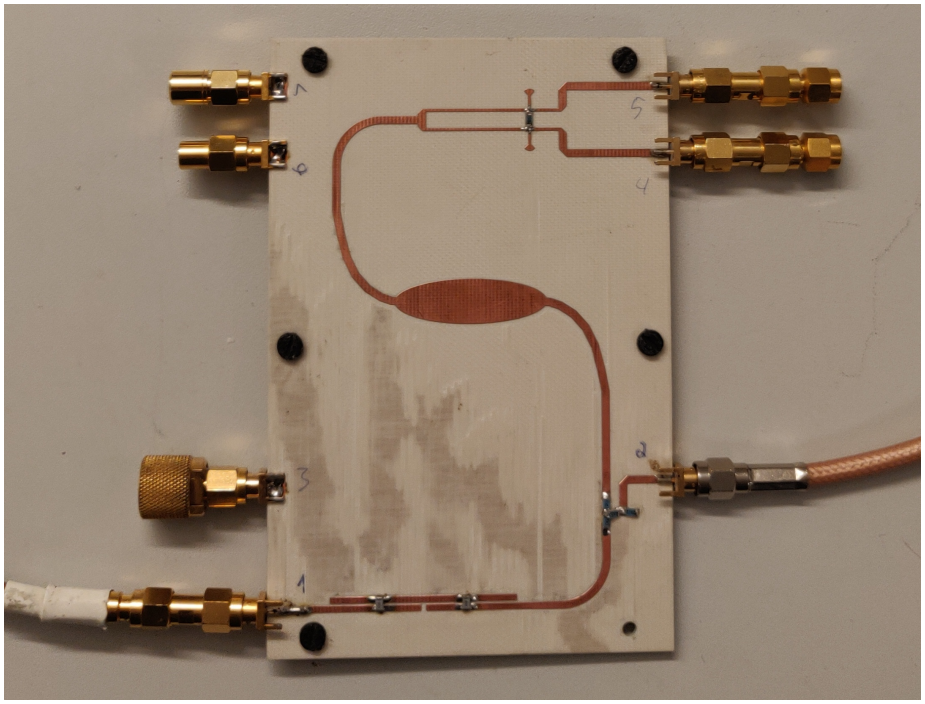

Figure 7.6: The setup for measuring the S21 parameter of the TX-module. The ports not measured are terminated with 50Ω loads.

Chapter 8

Filter optimization

In order to effectively cancel the SI introduced by the reflections in the Tx-module, a multi-tap filter was used. The filter has $3N$ degrees of freedom, where N is the number of taps. These parameters need to be optimized for the signal the filter is cancelling. This was done using a model of the filter implemented in Python using equation (3.3). To optimize this filter model, the basin-hopping algorithm was used with the Nelder-Mead downhill simplex algorithm, both algorithms implemented in the Python package SciPy [24].

The SciPy implementation of the basin-hopping and Nelder-Mead algorithm minimizes a function returning a scalar. An objective function was constructed, where the difference in magnitude and phase of the filter frequency response is compared to the received signal phase shifted 180° using equations (8.1) and (8.2).

$$\Delta_{\text{mag}}(\omega j) = |H_{canc}(\omega j)| - |H_{rx}(\omega j)| \tag{8.1}$$

$$\Delta_{\text{phase}}(\omega j) = \tan^{-1}\left(\frac{Re(H_{canc})}{Im(H_{canc})}\right) - \left(\tan^{-1}\left(\frac{Re(H_{rx})}{Im(H_{rx})}\right) + \pi\right) \tag{8.2}$$

In order for the algorithm to evaluate the fit for the current iteration, the sum of diffrences squared over the frequency band was calculated using equation (8.3).

$$Er = \sum_{\omega_{min}}^{\omega_{max}} \Delta^2_{\text{mag}}(\omega j) + \Delta^2_{\text{phase}}(\omega j), \tag{8.3}$$

where ω_{min} and ω_{max} are the frequency range the filter is optimized over.

The minimization algorithm uses an initial guess in order to perform the minimization. To decrease the iterations needed to find the global minimum an initial guess close to the actual global minimum was used.

The initial guess for the filter parameters was found visually by plotting the time domain response of the filter against the received time signal and manually selecting attenuation, delay and phase parameters, shown in figure 8.1.

The basin-hopping minimization was run for 20000 hops with approximately 10 million calls of the objective function. To minimize the computational time, the objective function was optimized and parallelized using the Python package Numba [25]. This decreases the time each call of the objective function from 0.0019 s to 0.00049 s. By using Numba the number of hops in the basin-hopping

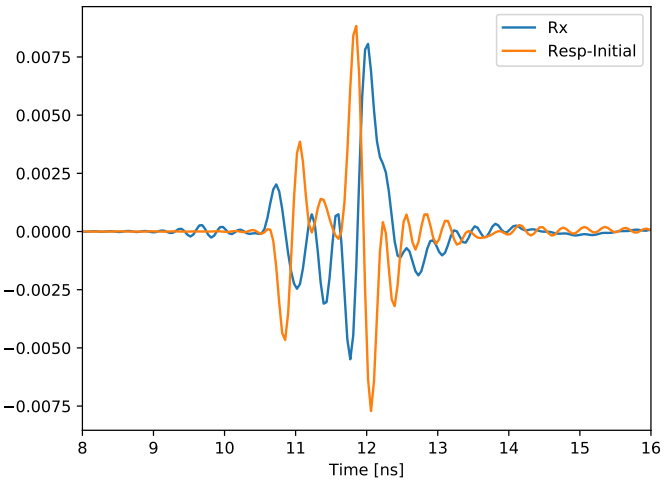

Figure 8.1: Time domain plot of the filter response with the initial guess of a two tap filter parameters

algorithm could be increased yielding a better estimation of the global minimum with no increase to the computational time.

Three filters with, 2, 3 and 4 taps were optimized in order to determine the optimum number of taps.

Chapter 9

Filter module design

9.1 Power divider

An Owens power divider was selected to split the signal to the two taps. This gave both good isolation between the two taps and replaced the attenuator for each tap. By selecting the coupling between the input and each of the outputs such that the power for each tap was attenuated equal to the optimized filter parameters. To combine the taps, a Wilkinson power divider with radial stub was utilized.

The Owens power divider have a attenuation of -6.1dB for the first tap and -1.6dB for the second tap in addition to the split.

9.2 Phase shifter

Three different phase shifter designs were investigated; the broadside coupled line, the edge coupled line and the parallel stub phase shifter. The structures were modeled in CST Microwave Studio, this allowed for the optimization of the parameters to achieve the desired phase shift while reducing the insertion and return loss. To calculate the differential phase shift introduced by the phase shifters, a reference microstrip line was simulated along side the phase shifters. This reference line had the same linear phase shift as the phase shifters. To optimize for the differential phase shift the phase data from the phase shifter and the reference line were unwrapped giving the total phase shift not limited to $\pm 180°$. The unwrapped reference phase was then subtracted from the phase shifter to calculate the differential phase shift.

9.2.1 Edge coupled phase shifter

The optimization of the edge coupled line phase shifter did not yield the desired phase shift. This was a result of the optimized parameters for a 23.95° differential phase shift not being able to fabricate with a spacing between the transmission lines less than 0.1 mm. By limiting the gap to no less than 0.1 mm the structure was not able to achieve the desired phase shift with acceptable insertion and return losses.

9.2.2 Broadside coupled phase shifter

The broadside coupled phase shifter did achieve a differential phase shift of 24° at the center frequency of 2GHz, but with a large deviation in the phase shift throughout the bandwidth. By taking phase shift deviation and the increased complexity of the construction into consideration the broadside coupled phase shifter was discarded in favor to the parallel stub phase shifter.

9.2.3 Parallel stub phase shifter

The parallel stub phase shifter was first simulated using the schematic designer in CST Microwave Studio. This allowed for quicker initial parameter estimation than full wave simulation. The schematic simulation utilises pre built models of microstrip lines, junctions and open/shorted stubs. Where the models for the microstrip lines only used the width and length of the line and the thickness and dielectric constant for the substrate.

The estimated parameters where then used to produce a 3D model of the phase shifter using 0.81 mm thick RO4003C substrate. The full wave simulation of the modeled phase shifter did not yield the same performance as the schematic based simulation as expected. The modeled phase shifter was optimized using the full wave simulation, giving the optimized parameters for the parallel stub phase shifter with 24° differential phase shift: $L_m = 20.51$ mm, $W_m = 2.174$ mm, $W_{s1} = 0.231$ mm, $W_{s2} = 0.122$ mm, $L_{s1} = 2.428$ mm, $L_{s2} = 22.728$ mm.

To decrease the phase shifter footprint a bend was introduced into the shorted stub, this change the impedance and the final structure with the bent stub was optimized one final time, giving the final parameters for the phase shifter: $L_m = 20.51$ mm, $W_m = 2.385$ mm, $W_{s1} = 0.123$ mm, $W_{s2} = 0.270$ mm, $L_{s1} = 3.416$ mm, $L_{s2} = 24.10$ mm.

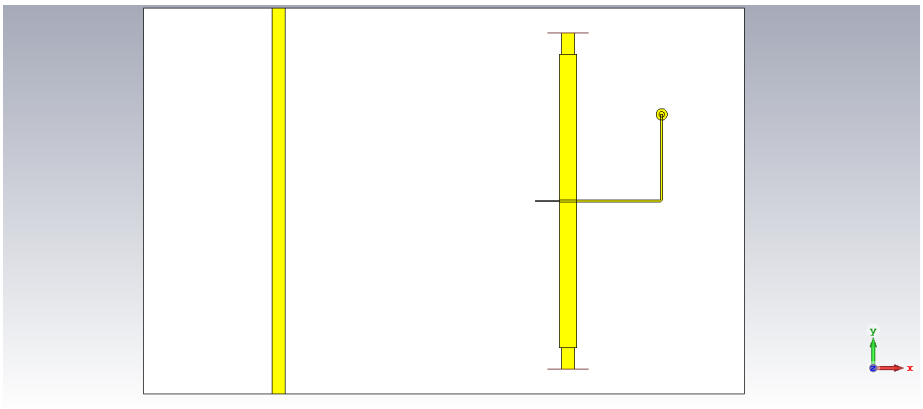

Figure 9.1

9.3 Delay line

The time delay of the filter is dependent on the delay line and all the transmission lines between port 3 of the Tx-module and the output port of the filter.

The shared time delay for the taps is introduced by the cable connecting the Tx-module, the microstrip line from the connector to the Owens divider and the Wilkinson power divider used for combining the signals from the tap.

The time delay introduced by the coaxial cable produced by Micro Circuits used was measured using a Agilent DSA-X 91304A. To measure the delay a stepped signal split to the two channels using a power splitter. The cables used after the power splitter needed to be calibrated for. The base delay difference between the cables used in the measurement was 4 ps. The measured delay of coaxial cable used to connect the Tx-module and the filter-module was 276 ps.

From the simulated results the delay of the Owens and Wilkinson power dividers are, 157 ps and 306 ps, respectively. This gives total delay for both taps of 739 ps.

Based on the result of the optimized filter parameters the delay for tap 1 and 2 are 0.855 ns and 1.629 ns.

The first tap needs a transmission line with a delay of 116 ps. The length of microstrip line that results in 116 ps time delay is 21.34 mm, while the length of a stripline is 18.91 mm. A microstrip delay line was chosen for this tap since the stripline does not save space on the board with the required microstrip to stripline transitions.

This length of microstrip line was used to connect the output of the Owens power divider used for this tap directly to the wilkinson power divider used to combine the taps.

To verify the correct length of the tap, the partially complete filter was modeled and the full wave propagation through the tap was simulated. The ports of the power divider and adder used for the second tap was terminated during the simulation.

The total delay of the second tap was additionally affected by the time delay caused by the phase shifter.

The length of delay line for the second tap was determined by simulating a complete filter-module with a straight 20 mm stripline delay line. The simulated model included the transitions between the microstrip lines and the striplines. This resulted in less than the needed delay. This difference in delay was used to calculate the final length of the meandering stripline segment. The length of the required stripline delay line was 66.14 mm, this length was achieved using a meandering line to minimize the size of the filter board.

Figure 9.2: A screenshot from the Agilent DSA-X91304A digital signal analyzer. The measured delay is 280 ps including the base delay difference introduced by the cables used in the measurement setup.

9.4 Fabricated filter module

The filter module was fabricated using the same 0.81 mm Rogers RO4003C substrate as the Tx-module. The narrow stubs in the phase shifter with only a width 0.123 mm and 0.270 mm made the fabrication of the board difficult. In the time between the fabrication of the Tx-module and the filter module, the cut depth of the PCB mill used to fabricate the boards was changed. This caused the mill to cut traces narrower than modeled, the deviation in trace width was -0.2 mm. This caused the narrow stubs to separate of the substrate. To compensate for the calibration error the trace width was widen by 0.2mm, resulting in the correct trace width. The fabricated filter module with the cable used to connect the modules together is shown in figure 9.3

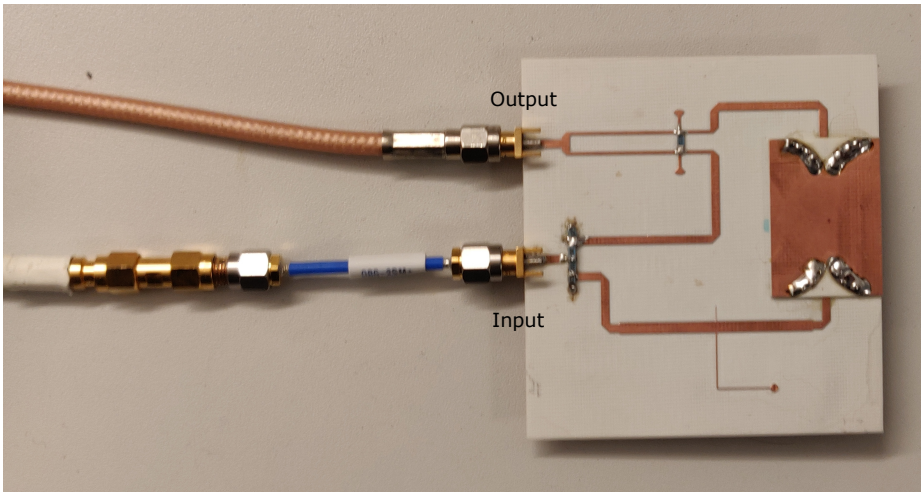

Figure 9.3: Fabricated filter-module with the cable used for connecting the Tx-module with the filter-module

Chapter 10

Complete system measurement

To measure the complete system the Agilent FieldFox N9916A VNA was used, the measurement setup is shown in figure 10.1. The output of the VNA is connected to the input of the Tx-module. The Tx-module and filter-module was connected together with the coaxial cable the filter was designed for. The antenna outputs of the Tx-module was terminated with 50Ω loads. The reaming output of the Tx-module and the output of the filter-module was connected to a power combiner. The input of the VNA was connected to the output of the power combiner. The cables connecting the outputs to the power combiner were of the same length, to prevent any differential delay between the outputs. The power combiner used was produced by Mini-Circuits with model number ZN2PD2-14W-S+.

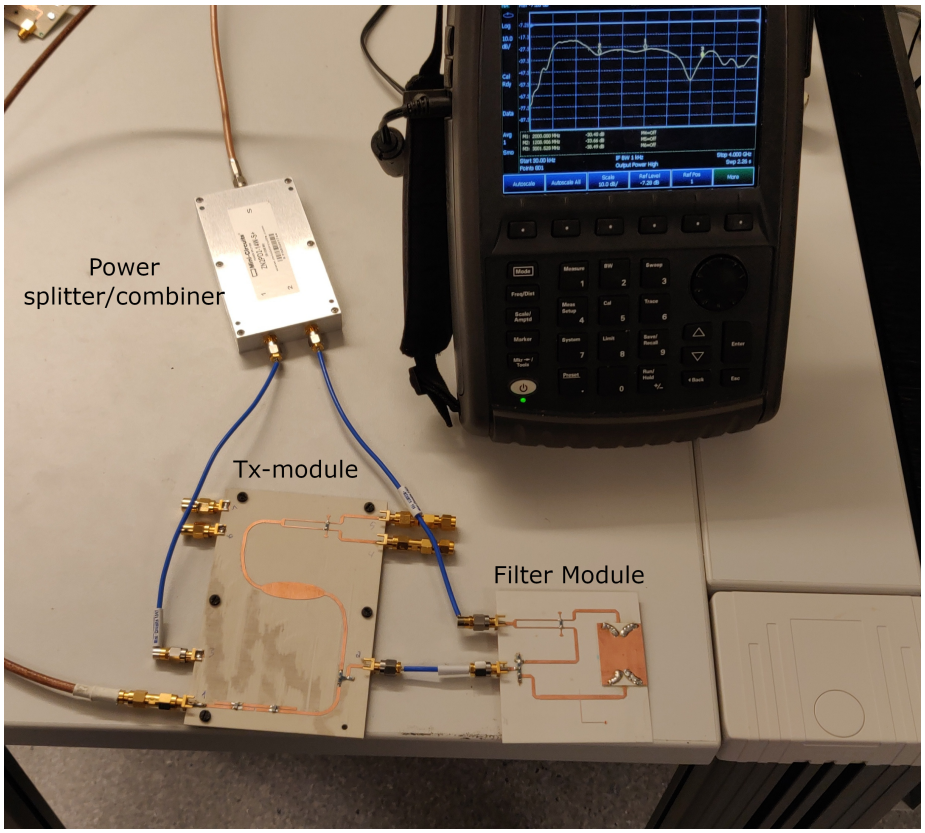

Figure 10.1

Part III

Results and discussion

Chapter 11

Tx-module

11.1 Component simulation results

11.1.1 Bandpass filter

Figure 11.1 shows the S-parameters for the bandpass filter. The return and insertion loss is low in the frequency band of 1-3GHz, while outside the band they are high with the almost all the power being reflected. This is the expected result for a bandpass filter.

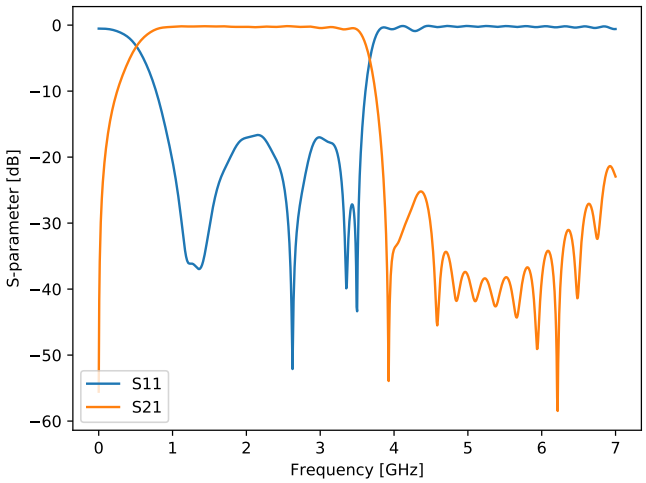

Figure 11.1: The simulated S-parameter for the 1-3GHz bandpass filter.

11.1.2 Unequal divider

Figure 11.2 shows the S-parameters for the unequal power divider. The output power at port 2 is at -35dB while the power at port 3 is -15dB for the entire frequency band. The return loss in the frequency band is lower than -16dB. The S21 and S31 parameters are not affected by the frequency and flat in the frequency band. This is the expected results for a resistive divider where the effective frequency band extends down to 0Hz.

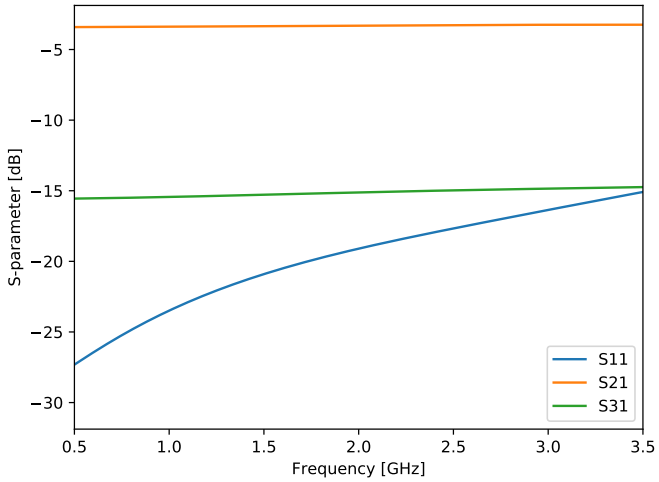

Figure 11.2: S-parameters for the unequal power divider with attenuation 3dB and 15dB.

11.1.3 Power dividers

Figure 11.3 shows the S-parameters for the wye and Wilkinson power divider. The Wye power divider has a output power of -6 dB over the frequency band, which corresponds with the calculated power division. The Wilkinson power divider with radial stubs has a output power of -3.5 dB which is close to the theoretical -3 dB power split. Based on these results it is visible that the Wilkinson power divider is a better fit for the Tx-module. By using the Wilkinson power divider more power is transmitted to the antennas. The increased reflection loss of the Wilkinson power divider compared to the Wye divider can be cancelled using the SIC-filter.

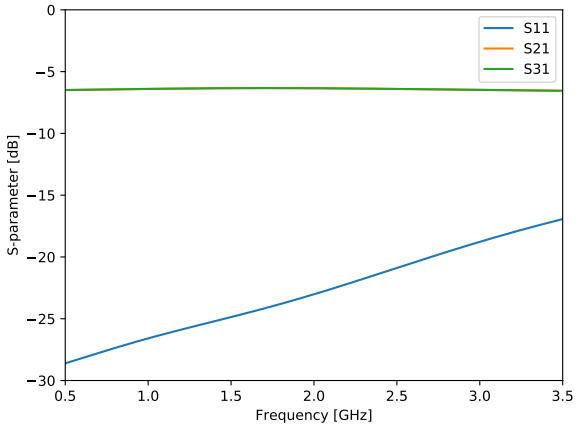

(a)

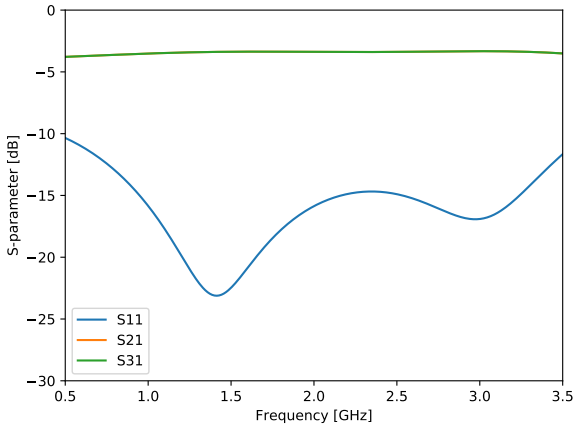

(b)

Figure 11.3: The simulated S-parameters for two equal split power dividers. (a) Wye. (b) Wilkinson with radial stub.

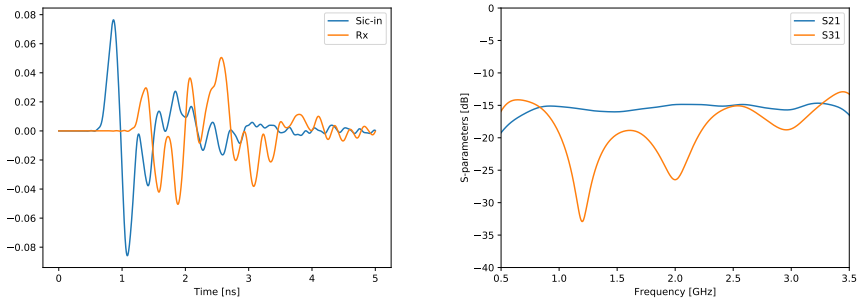

(a) **(b)**

Figure 11.4: S-parameter simulated Tx-module. (a) Time domain signal. (b) S-parameters.

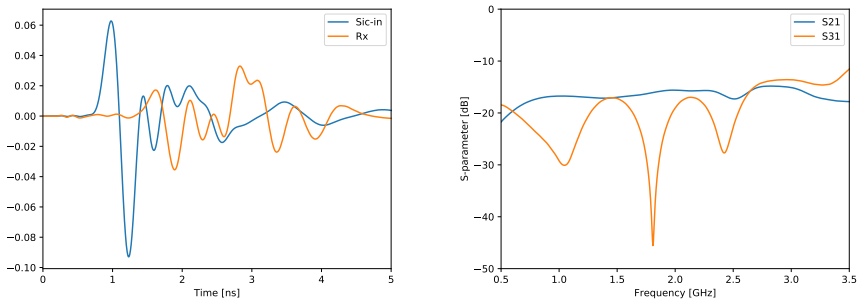

(a) **(b)**

Figure 11.5: Simulated full Tx-module. (a) Time domain signal. (b) S-parameters.

11.1.4 Tx-module simulations

Figure 11.4 shows the simulated time domain signal and S-parameters. The Rx signal is noise present in the front end, while the Sic-in signal is the input to the filter used to cancel the Rx noise. The time domain response is as expected, with little delay between the input and outputs since no microstrip lines are connecting the components.

Figure 11.5 shows the resulting time domain signal and S-parameters. Compared to the S-parameters simulation the time domain signals is spread out in time with increased delay between them. This is cause by the transmission lines connecting the components. Due to this delay the noise is clearly separated into two pulses, where the first is the directly coupled signal into the isolated port of the directional coupler. While the second one is the power reflected by the power dividers. In figure 11.4 these reflections are not separated in time to the same extent. To cancel this more complex noise a filter with more taps are needed compared to the simpler noise signal in figure 11.5.

11.2 Measured Tx-module results

Figure 11.6 shows the S-parameters as well as the reconstructed time signal. The time signal is reconstructed by the use of the inverse Fourier transform. The noise signal is similar to the simulated Tx-module, with the noise consisting of the same two noise signals. The power of the extracted signal is closer to the calculated power split then the simulated signal.

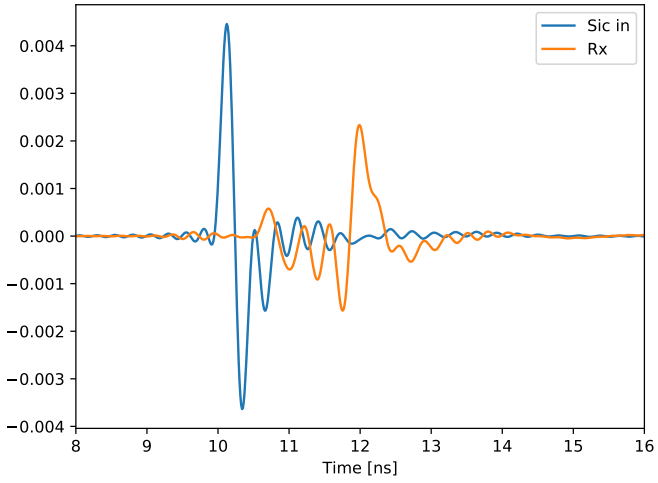

(a)

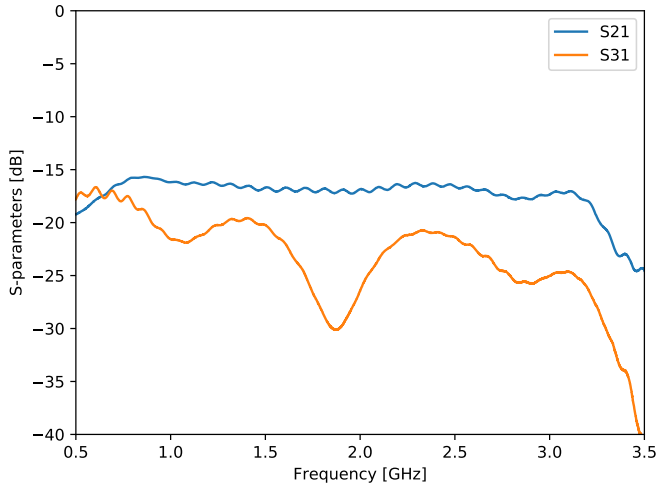

(b)

Figure 11.6: The measured reconstructed time domain signal (a) and S-parameters (b).

Chapter 12

Filter parameter optimization results

The time and frequency domain response for the three optimized filters are shown in figure 12.1. The optimized filter with two taps have an average cancellation of 14.42 dB over the frequency band. The optimized 3 and 4 tap filters had lower average cancellation but higher maximum. Based on the optimized 2, 3 and 4 tap filters, the 2 tap filter was chosen for fabrication, due to the better average cancellation and simpler design to realise. The first tap of the chosen 2-tap filer have the parameters; 0.855 ns delay, 0° phase shift and a attenuation ratio of 0.50. The second tap have 1.628 ns delay, 24° phase shift and a attenuation ratio of 0.84.

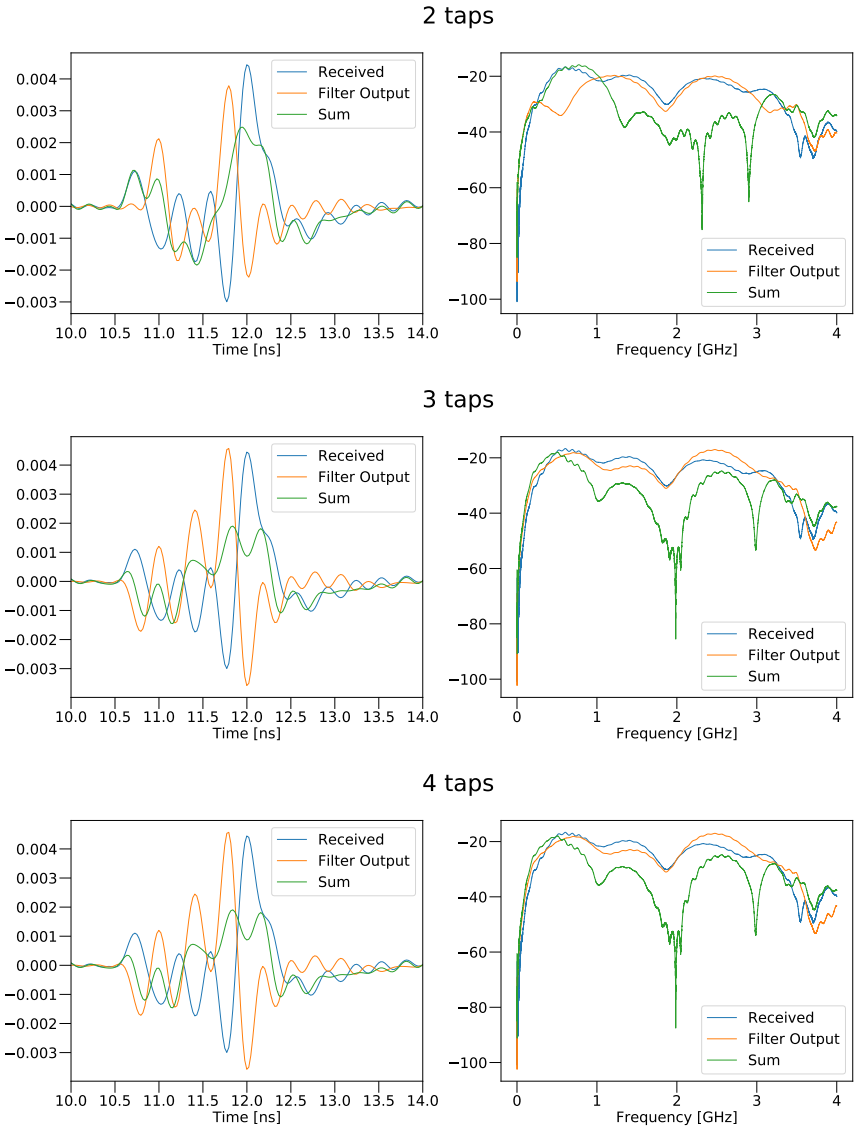

Figure 12.1: The time and frequency domain response for three optimized multi-tap filters with 2, 3 and 4 taps

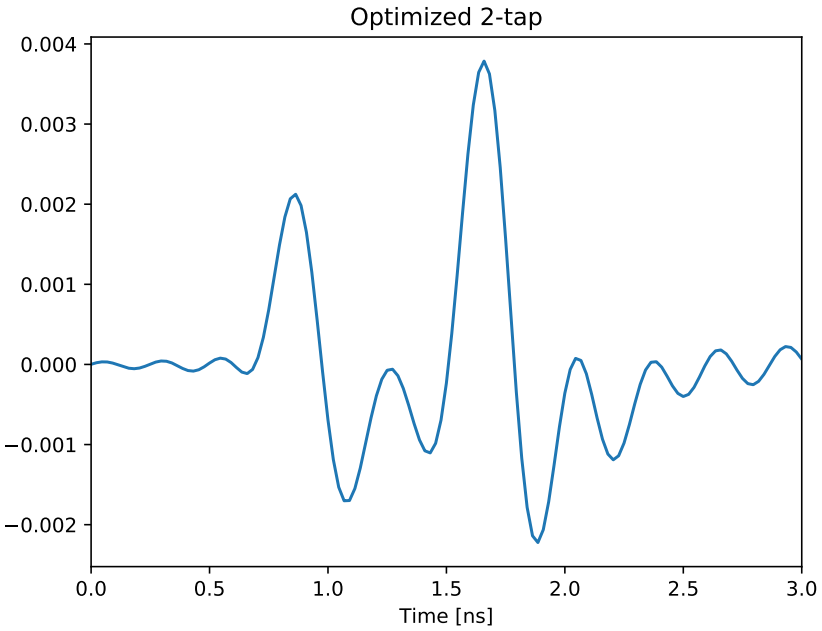
Optimized 2-tap
0.004
0.003
0.002
0.001
0.000
−0.001
−0.002
0.0
0.5
1.0
1.5
2.0
2.5
3.0
Time [ns]

Figure 12.2

Chapter 13

Filter module results

13.1 Simulated components

13.1.1 Owens power divider

The simulated Owens power divider has 12 dB attenuation on the first tap and 8 dB attenuation on second tap. This is lower than the optimized filter parameters and is a result of the included loss in the Owens divider. This was later compensated for in the fabricated filter module by changing the resistance values in the power splitter.

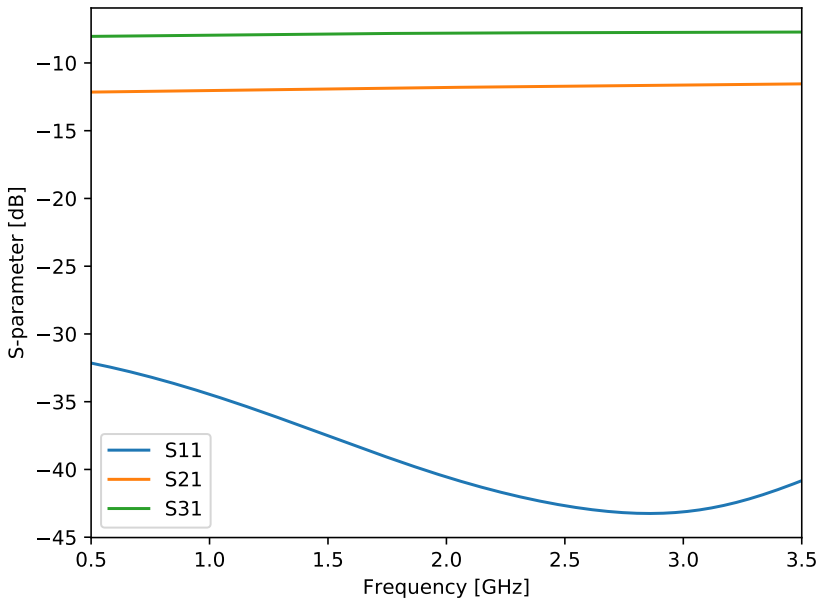

Figure 13.1

13.1.2 Phase shifter

The optimized parallel stub phase shifter has a low loss, with an insertion loss of -1 dB and a reflected loss lower than -10 dB, shown in figure 13.2. The phase shifter have a differential phase shift of 24° with a phase deviation, shown in figure 13.3, of ±1.5°. This is a acceptable phase deviation for the multi-tap filter designed.

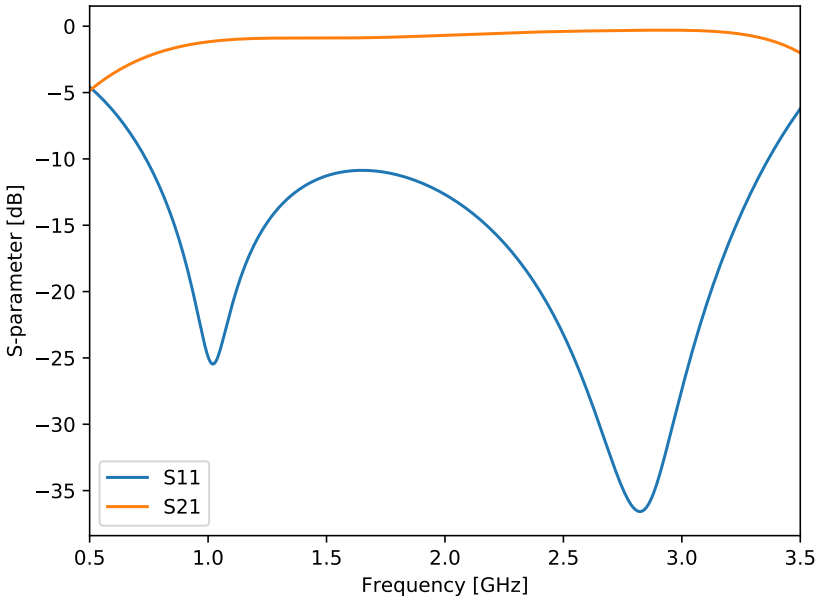

Figure 13.2: The simulated S-parameters for the parallel stub phase shifter.

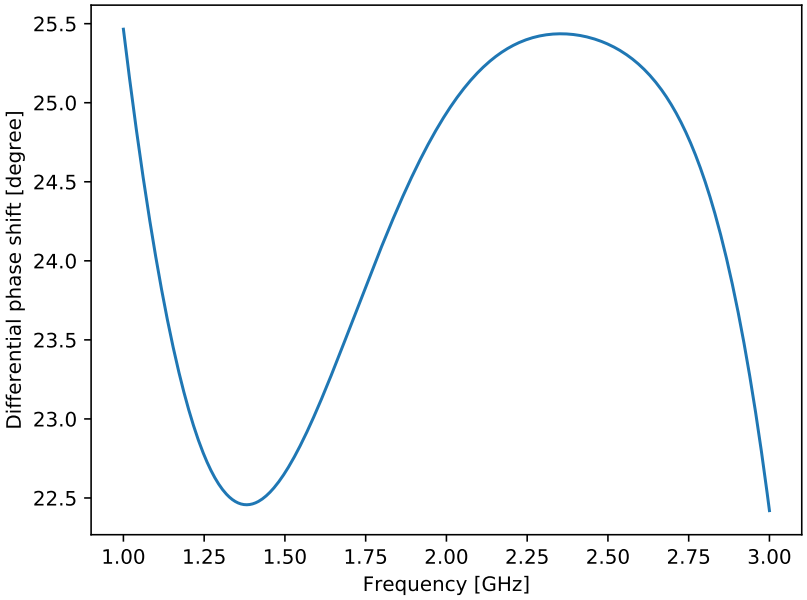

Figure 13.3: The simulated differential phase shift for the parallel stub phase shifter.

13.1.3 Delay line

Figure 13.4 show the simulated filter module excited using a step function. In the plots two steps are visible, the first step is the signal from the first tap with the shortest delay. The second step is the longer tap with longer delay and phase shifter. The initial filter module with 20 mm stripline delay line has a total delay of 1.125 ns. Adding the additional cable delay of 276 ps the total delay of the tap is 1.401 ns.

The by changing the 20 mm straight stripline to a 66.14 mm meandering line the total delay was brought up to 1.674 ns.

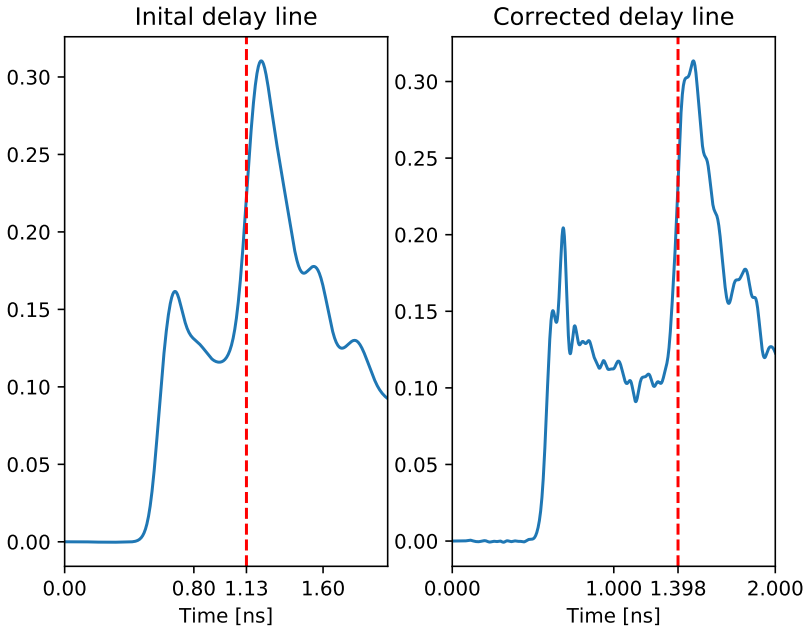

Figure 13.4

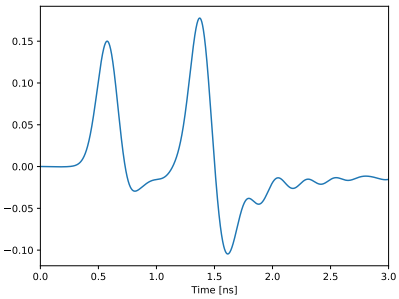

(a)

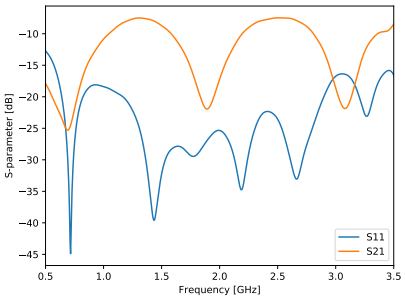

(b) The simulated complete filter-module. (a) Time domain signal. (b) S-parameters

Figure 13.5

13.1.4 Complete module

Figure 13.5 show the simulated time and frequency domain results for the complete filter-module. Compared to the 2-tap optimized filter, figure 12.2, the filter has to similar taps. The taps have the same time delay and close to the same phase shift as the optimized filter. The main difference is in the attenuation, both taps have more attenuation than the optimized filter. This was expected because of the power loss of the Owens power divider.

13.2 Measured filter module results

The measured time and frequency domain results of the fabricated filter module with the additional coaxial cable is shown in figure 13.6. The time and frequency response is on par with the simulated results. With the same delay, phase shift and attenuation.

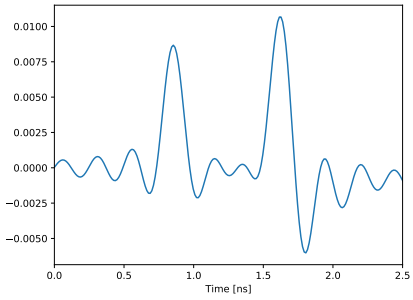

(a)

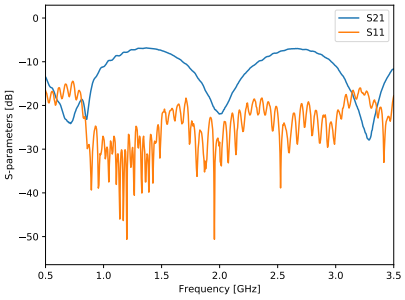

(b)

Figure 13.6: The measured fabricated filter-module. (a) Time domain signal. (b) S-parameters.

Chapter 14

Complete system

The measured complete system with a 15 dB attenuation of the filter input signal is shown in figure 14.1. The measurements show a reduction in the received power in the frequency band of 1-3 GHz. The average power reduction in in frequency band is 8.01 dB, with a maximum of 27.76 dB at 2.8 GHz. This is considerably lower cancellation than the optimized filter with a average of 14.42 dB. This is a result of the additional attenuation in the filter-module. By inspecting the time domain response it is visible that the power of the second tap can be increased to achieve higher cancellation. To increase the cancellation the unequal power divider in the Tx-module was changed from a power split of 3.5 dB to 15.5 dB attenuation, to a power split of 4 dB to 12 dB. To compensate for the increase of input power the attenuation of the first tap was changed to -20dB. The resulting cancellation after the changes is shown in figure 14.2. The average cancellation for the final system is 10.45dB, with a maximum of 38.71dB at 1.17GHz. The cancellation is still lower than the optimized filter, this is a product of deviation in filter parameters compared to the optimized filter.

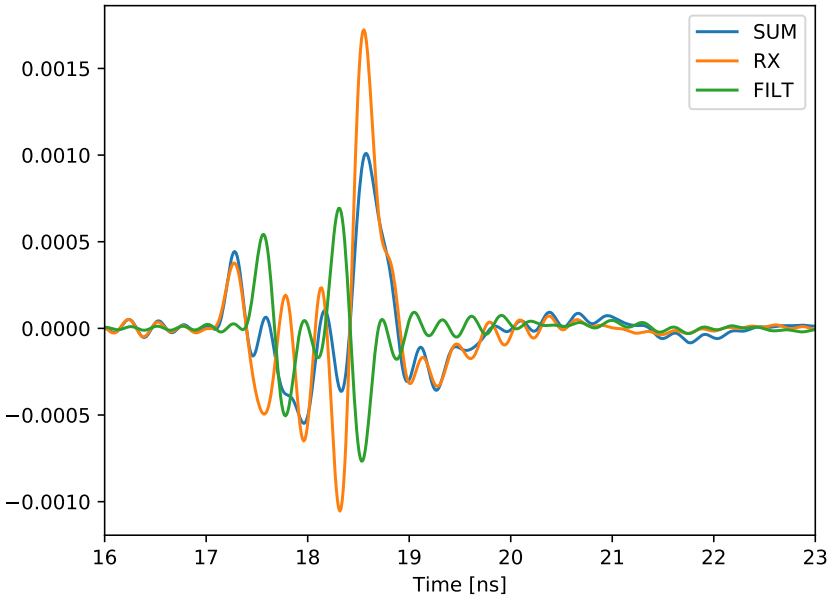

(a)

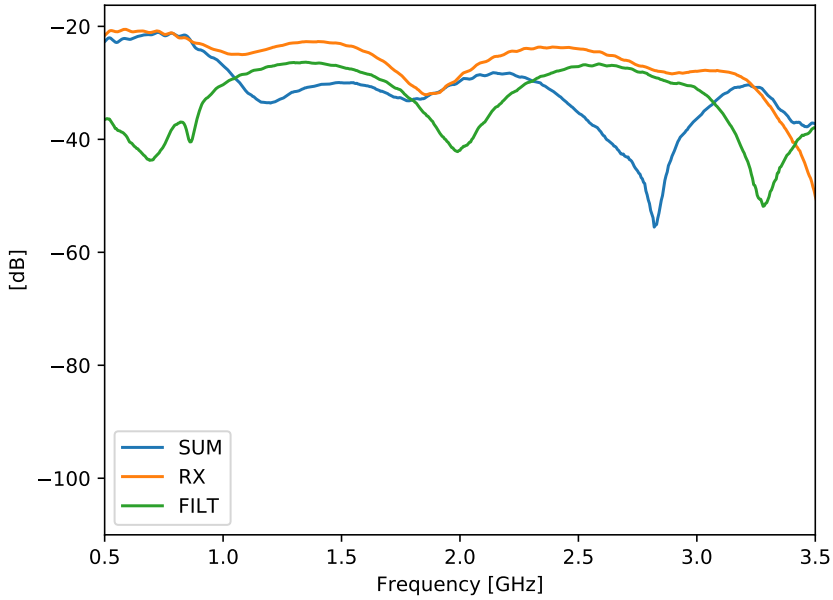

(b)

Figure 14.1

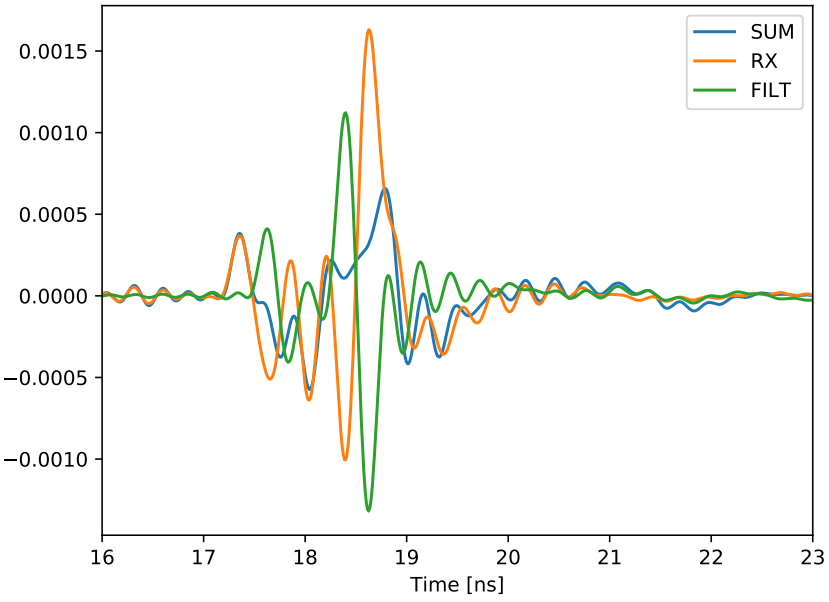

(a)

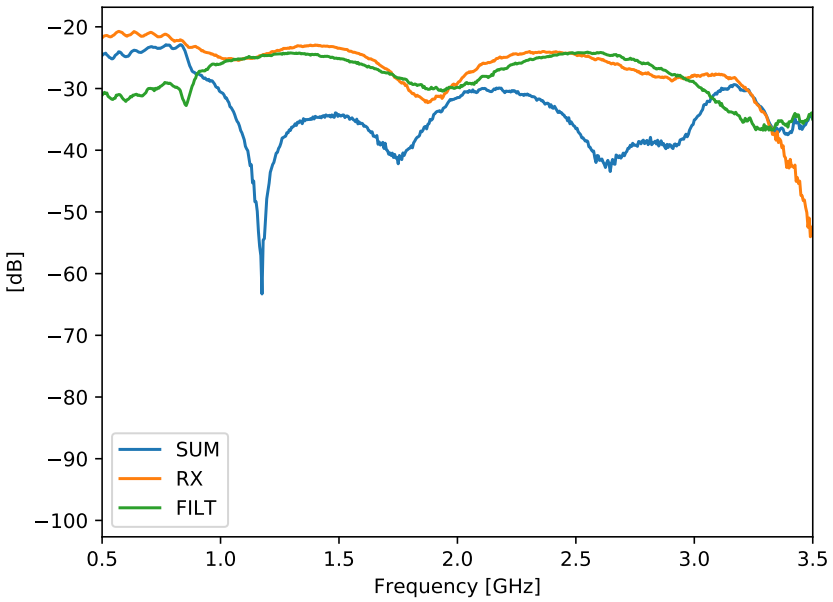

(b)

Figure 14.2

Part IV

Chapter 15

Conclusion

In this thesis a radar front-end containing a self-interference cancellation filter was designed, simulated and fabricated. The final front-end consisted of two separate modules, a Tx-module and a filter-module. The cancellation filter was a multi-tap filter design, with phase shift, attenuation and delay elements. The filter parameters were optimized using the basin-hopping algorithm combined with the Nelder-Mead downhill simplex algorithm.

The Tx-module contained a bandpass filter, a unequal power divider, a directional coupler and two power dividers. The filter-module contained a 2-tap cancellation filter, consisting of a unequal split Owens power divider, a parallel stub phase shifter, a stripline delay line with microstrip to stripline transitions and a Wilkinson power divider with radial stubs to extend the bandwidth. The designed Wilkinson power divider had a functional band width of 1-3 GHz with 3.5 dB insertion loss. The designed parallel stub phase shifter had a differential phase shift of 24° with a phase deviation of ±1.5° over the frequency band 1-3 GHz. In addition to the parallel stub phase shifter two additional phase shifter designs was explored.

The constructed cancellation filter resulted in a average of 10.45 dB power reduction over the frequency band of 1-3 GHz.

Chapter 16

Bibliography

[1] M. I. Skolnik, *Introduction to radar systems*. Boston: McGraw Hill, 3rd ed. ed., 2001.

[2] K. E. Kolodziej, J. G. McMichael, and B. T. Perry, "Multitap rf canceller for in-band full-duplex wireless communications," *IEEE Transactions on Wireless Communications*, vol. 15, pp. 4321–4334, June 2016.

[3] S. Bojja Venkatakrishnan, E. A. Alwan, and J. L. Volakis, "Wideband rf self-interference cancellation circuit for phased array simultaneous transmit and receive systems," *IEEE Access*, vol. 6, pp. 3425–3432, 2018.

[4] S. Mercier, D. Roque, and S. Bidon, "Successive self-interference cancellation in a low-complexity wcp-ofdm radar receiver," in *2018 52nd Asilomar Conference on Signals, Systems, and Computers*, pp. 712–716, 2018.

[5] D. Pozar, *Microwave Engineering*. Wiley, 2012.

[6] I. J. Bahl and R. Garg, "A designer's guide to stripline circuits," *Microwaves*, pp. 90–96, January 1978.

[7] M. V. Schneider, "Microstrip lines for microwave integrated circuits," *The Bell System Technical Journal*, vol. 48, no. 5, pp. 1421–1444, 1969.

[8] E. O. Hammerstad, "Equations for microstrip circuit design," in *1975 5th European Microwave Conference*, pp. 268–272, Sep. 1975.

[9] H. A. Wheeler, "Transmission-line properties of parallel strips separated by a dielectric sheet," *IEEE Transactions on Microwave Theory and Techniques*, vol. 13, no. 2, pp. 172–185, 1965.

[10] S. Hong, J. Brand, J. I. Choi, M. Jain, J. Mehlman, S. Katti, and P. Levis, "Applications of self-interference cancellation in 5g and beyond," *IEEE Communications Magazine*, vol. 52, no. 2, pp. 114–121, 2014.

[11] D. Adams, "Designing resistive unequal power dividers," *High Frequency Electronics*, March 2007.

[12] C. Owen, "Owen splitter microwave 101." `https://www.microwaves101.com/encyclopedias/owen-splitter`, Jan 2007. Accessed: November 13 2020.

[13] E. J. Wilkinson, "An n-way hybrid power divider," *IRE Transactions on Microwave Theory and Techniques*, vol. 8, no. 1, pp. 116–118, 1960.

[14] B. Mishra, A. Rahman, S. Shaw, M. Mohd, S. Mondal, and P. P. Sarkar, "Design of an ultra-wideband wilkinson power divider," in *2014 First International Conference on Automation, Control, Energy and Systems (ACES)*, pp. 1–4, 2014.

[15] H. Habibi and H. M. Naimi, "Taper transmission line uwb wilkinson power divider analysis and design," *International Journal of Electronics*, vol. 106, no. 9, pp. 1332–1343, 2019.

[16] O. Ahmed and A. R. Sebak, "A modified wilkinson power divider/combiner for ultrawideband communications," in *2009 IEEE Antennas and Propagation Society International Symposium*, pp. 1–4, 2009.

[17] A. M. Abbosh and M. E. Bialkowski, "Design of compact directional couplers for uwb applications," *IEEE Transactions on Microwave Theory and Techniques*, vol. 55, no. 2, pp. 189–194, 2007.

[18] S. Y. Zheng, W. S. Chan, and K. F. Man, "Broadband parallel stubs phase shifter," in *2009 Asia Pacific Microwave Conference*, pp. 1368–1371, 2009.

[19] L. Guo, H. Zhu, and A. Abbosh, "Wideband phase shifter with wide phase range using parallel coupled lines and l-shaped networks," *IEEE Microwave and Wireless Components Letters*, vol. 26, no. 8, pp. 592–594, 2016.

[20] L. Guo and A. Abbosh, "Phase shifters with wide range of phase and ultra-wideband performance using stub-loaded coupled structure," *IEEE Microwave and Wireless Components Letters*, vol. 24, no. 3, pp. 167–169, 2014.

[21] T. Maleszka and G. Jaworski, "Broadband stripline to microstrip transition with constant impedance field matching section for applications in multilayer planar technologies," in *18-th INTERNATIONAL CONFERENCE ON MICROWAVES, RADAR AND WIRELESS COMMUNICATIONS*, pp. 1–4, 2010.

[22] J. A. Nelder and R. Mead, "A Simplex Method for Function Minimization," *The Computer Journal*, vol. 7, pp. 308–313, 01 1965.

[23] *CST Microwave Studio*, 2020. https://www.cst.com.

[24] P. Virtanen, R. Gommers, T. E. Oliphant, M. Haberland, T. Reddy, D. Cournapeau, E. Burovski, P. Peterson, W. Weckesser, J. Bright, S. J. van der Walt, M. Brett, J. Wilson, K. J. Millman, N. Mayorov, A. R. J. Nelson, E. Jones, R. Kern, E. Larson, C. J. Carey, İ. Polat, Y. Feng, E. W. Moore, J. VanderPlas, D. Laxalde, J. Perktold, R. Cimrman, I. Henriksen, E. A. Quintero, C. R. Harris, A. M. Archibald, A. H. Ribeiro, F. Pedregosa, P. van Mulbregt, and SciPy 1.0 Contributors, "SciPy 1.0: Fundamental Algorithms for Scientific Computing in Python," *Nature Methods*, vol. 17, pp. 261–272, 2020.

[25] S. K. Lam, A. Pitrou, and S. Seibert, "Numba: A llvm-based python jit compiler," in *Proceedings of the Second Workshop on the LLVM Compiler Infrastructure in HPC*, LLVM '15, (New York, NY, USA), Association for Computing Machinery, 2015.